ROYAL SOCIETY
OF CHEMISTRY

PAPER

Check for updates

Co-spray printing of LiFePO$_4$ and PEO-Li$_{1.5}$Al$_{0.5}$Ge$_{1.5}$(PO$_4$)$_3$ hybrid electrodes for all-solid-state Li-ion battery applications†

Junfu Bu, [ID] *[ab] Puiki Leung,[a] Chun Huang, [ID] [a] Sang Ho Lee [ID] [a] and Patrick S. Grant*[ab]

LiFePO$_4$ (LFP) electrodes for Li-ion battery applications were prepared by spray printing. By optimising the substrate temperature, solvent ratio and electrode material concentration, a honeycomb pore structure was produced over a large area electrode. In a liquid electrolyte, the honeycomb structured LFP electrode showed improved cycling performance at high C-rate due to shortened pore pathways and improved Li mobility. In a solid-state configuration, a PEO(LITFSI)-Li$_{1.5}$Al$_{0.5}$Ge$_{1.5}$(PO$_4$)$_3$ (PEO-LAGP) based solid electrolyte was either spray printed on top of the LFP and/or interleaved within sub-layers of the LFP electrode, for both non-honeycomb and honeycomb pore morphologies. Cross-sectional scanning electron microscope (SEM) and energy-dispersive X-ray spectroscopy (EDS) mapping combined with electrochemical impedance spectroscopy (EIS) testing showed that the honeycomb electrode with inter-leaved sub-layers of solid-state electrolyte improved interfacial contact between the electrode and electrolyte. When coupled with Li foil in a solid-state Li ion battery configuration, the honeycomb interleaved electrode also showed the best performance in terms of capacity and cycle stability at all testing temperatures, showing capability that exceeded previously reported performance.

Introduction

Greater market penetration of electric vehicles (EVs) and hybrid electric vehicles (HEVs) is required to reduce environmental pollution and the requirement for carbon-intensive fuels. Due to their excellent gravimetric energy density ($\sim$270 W h kg^{-1}), reducing cost ($\sim$US$100 kW h^{-1}) and widespread availability, lithium ion batteries (LIBs) have become the practical technology of choice for EVs and HEVs.[1–3] However, LIBs have relatively low power density ($\sim$250–340 W kg^{-1}) and slow charge for pure EV requirements.[4,5] Mass-market LIBs also use an organic solvent-based liquid electrolyte that is flammable potentially toxic and has poor chemical stability that, under certain conditions, can pose potential safety issues of leakage, fire or even explosion especially in large-scale energy storage systems.[6]

To promote higher power density, intrinsically higher speed lithium insertion materials (*e.g.* Li$_4$Ti$_5$O$_{12}$), porosity engineering (*e.g.* aligned pore channels through the electrode thickness), thinner electrodes (<50 μm), and many different types of nano-scale active materials have been suggested, but their practical implementation usually involves compromises in gravimetric energy density and/or volumetric energy density, or increased side and other reactions due to increased active material surface area.[7–10] Rather than the planar large area foil current collector-based electrodes used commercially, investigations of 3D electrode morphologies at the laboratory scale have also shown that faster ionic and electronic transport can be promoted, which supports faster charging and/or discharging performance.[11–18] However, these approaches are difficult to scale-up economically.

With regard to the safety concerns or restricted material choices associated with the relatively reactive liquid organic solvent-based electrolytes used in LIBs, solid-state batteries in which the liquid is replaced by a gel or solid ion conductor offer the possibility to improve safety and may enable the use of alkali metal (Li or Na) negative electrodes with unmatchable energy density.[19] Solid-state Li-ion electrolytes can be divided into inorganic (mainly ceramics) and organic (polymer), and great effort is being expended to develop these materials with ionic conductivities that approach those of organic liquid electrolytes (>10 mS cm^{-1}), and this has been extensively reviewed elsewhere.[20–25] Conductivity issues aside, for ceramic electrolytes, their lack of flexibility and low mechanical compliance creates significant difficulties in maintaining interfacial contact between the electrolyte and the entire surface of the active material in the electrode during intercalation/de-intercalation swelling and contraction. Their relatively high density can

[a]Department of Materials, University of Oxford, Parks Road, Oxford OX1 3PH, UK. E-mail: junfu.bu@materials.ox.ac.uk; patrick.grant@materials.ox.ac.uk

[b]Faraday Institution, Quad One, Harwell Campus, Didcot OX11 0RA, UK

† Electronic supplementary information (ESI) available. See DOI: 10.1039/c9ta03824h

19094 | *J. Mater. Chem. A*, 2019, **7**, 19094–19103

This journal is © The Royal Society of Chemistry 2019

also undermine the overall device gravimetric energy density.[26] Polymer electrolytes such as widely studied poly(ethylene oxide) (PEO) provide better mechanical compliance at electrolyte/active material interfaces but have insufficient structural stability to ensure anode–cathode separation while their relatively poor ionic conductivity in the range of 10^{-8} to 10^{-4} S cm^{-1} at ambient temperature also hinders their wider application.[20,27] Hybrid solid electrolytes composed of a dispersion of inorganic electrolyte particles in a polymer electrolyte matrix have been shown to offer a potentially attractive balance of ionic conductivity, interfacial compliance to maintain active/electrolyte interfacial contact, and structural rigidity.[28–30] However, challenges remain in reliably fabricating large area electrodes in which the hybrid electrolyte remains in intimate contact with all the available active material surface throughout repeated cycling.

This paper investigates a co-spray printing approach that prints thin layers of a LiFePO$_4$ (LFP) cathode material interlayered with thin layers of a PEO(LITFSI)-Li$_{1.5}$Al$_{0.5}$Ge$_{1.5}$(PO$_4$)$_3$ (PEO-LAGP) hybrid electrolyte. The layer-by-layer assembly of the electrode seeks to ensure the hybrid electrolyte is intimately and continuously dispersed to all parts of the electrode. As part of this aim, the spray printing of the LFP layers uses a bi-solvent drying phenomenon to promote through-layer honeycomb porosity so that the hybrid electrolyte penetrates both within and between layers.[31,32] By comparing various spray printed electrodes with identical fractions of active, inactive and electrolyte materials arranged in different geometrical configurations, we identify an optimum arrangement that delivers amongst the best reported performance for similar systems, and is achieved easily over large electrode areas of up to 20 × 20 cm or more. While the LFP cathode and hybrid PEO-LAGP electrolyte materials are used here to exemplify, the approach described is generic and similar benefits of interlayering in other cathode materials for solid-state batteries may be expected.

Results and discussion

The effects of spray printing parameters on electrode morphology

The role of key process parameters on the spray printed electrode microstructure was first investigated, including the effect of substrate temperature, suspension solvent ratio and suspension solid content.

Fabrication temperature. The boiling points of the NMP and IPA fugitive carriers were 202 °C and 82.6 °C respectively (NMP-based slurry cast LIB electrodes are usually dried at approximately 120 °C) and so a lower bound substrate temperature of 130 °C was chosen, with an upper bound temperature of 180 °C that was limited by the heated substrate capability. Fig. 1 shows scanning SEM images of a series of sprayed LFP-based electrodes as a function of temperature and otherwise identical conditions. A progressively more marked honeycomb pore morphology (diameter 1–5 μm) developed with increasing temperature. At 130 °C as shown in Fig. 1a, there were no pores while at 140 °C as shown in Fig. 1b some occasional large pores

had developed. When the electrode was prepared at 150 °C, there were more pores than at 130 °C and 140 °C but pores were irregular and randomly distributed. Between 160 and 180 °C as shown in Fig. 1d–f, changes in pore size and fraction were less marked and the porosity was more uniform. To show how the electrode microstructure and pores evolved, SEM images of foils sprayed with the LFP-based suspension after only 1, 2, 5, 10 and 20 spray cycles, or layers, are shown in Fig. S1,† for both substrate temperatures of 130 °C and 160 °C. After a single cycle, there was insufficient material for complete coverage and for both substrate temperatures, the particulates dried to form an inter-connected cellular pattern through which the underlying current collector could be seen. After subsequent deposition cycles at 130 °C, the pores were filled with particulates and a continuous coating was formed. In contrast at 160 °C and otherwise identical conditions, the pore structure formed in the first cycle was preserved as the electrode thickened with the characteristic honeycomb structure formed across the electrode, with pores of 1 to 5 μm. Fig. S2† shows a cross-sectional SEM image of a honeycomb electrode showing inter-connected pore channels preserved from the current collector through to the electrode surface. In addition, X-ray diffraction was used for confirm that there were no phase changes in the materials during the spray printing processing.

NMP/(NMP + IPA) ratio. The criticality of NMP and IPA fraction in the suspension is shown by the LFP-based electrode surface images in Fig. 2a to f, where the fraction of NMP was varied from 2.5 to 15 vol% in NMP + IPA, at a constant substrate temperature of 160 °C. All the electrodes showed the honeycomb structure but the porosity fraction decreased at 12.5 vol% NMP or greater (Fig. 2e and f). The honeycomb structure and the pore distribution at 10 vol% NMP (Fig. 2d) was more uniform than at other NMP ratio conditions. On the basis of Fig. 2 and 10 vol% NMP in NMP + IPA at a substrate temperature of 160 °C was chosen as the optimum condition to promote honeycomb pore arrays reproducibly over large current collector areas.[31,32]

Suspension solid content. The more concentrated the suspension, the greater the mass deposition rate and electrode formation rate, which is desirable from a technological point of view. However, concentrated suspensions may have poor
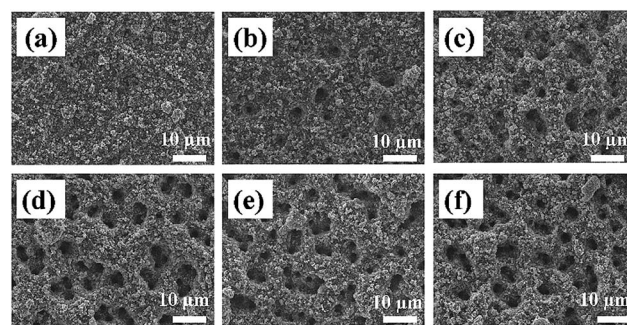

Fig. 1 SEM images of the surface of spray printed LFP-based cathodes as a function of substrate temperature (a) 130 °C, (b) 140 °C, (c) 150 °C, (d) 160 °C, (e) 170 °C and (f) 180 °C.
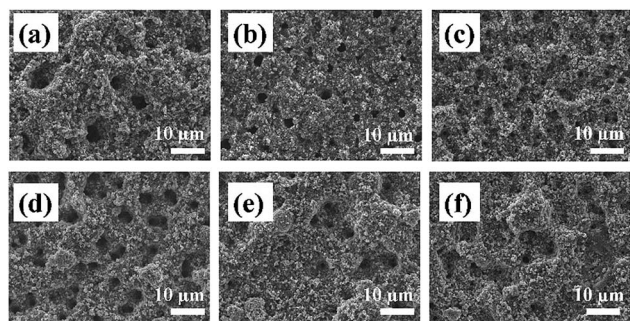
This journal is © The Royal Society of Chemistry 2019

J. Mater. Chem. A, 2019, **7**, 19094–19103 | **19095**

Fig. 2 SEM images of the surface of spray printed LFP-based electrodes at different NMP/(NMP + IPA) ratios of (a) 2.5 vol%, (b) 5 vol%, (c) 7.5 vol%, (d) 10 vol%, (e) 12.5 vol% and (f) 15 vol%.

stability that leads to a variable electrode structure and nozzle clogging. Fig. 3 shows a series of SEM images of the surface morphology of spray printed LFP-based electrodes where the total mass of solid in the suspension was varied from 0.05 to 0.5 g/100 ml of liquid. Below 0.15 g/100 ml, the desired pore structure did not form distinctly; above 0.3 g/100 ml, the honeycomb structure became less repeatable and coarse. Consequently, an optimum concentration of 0.25 g/100 ml was selected for subsequent experiments.

Electrochemical characterization

Liquid electrolyte based battery performance. Before investigating the LFP-based electrodes in a solid-state battery configuration, they were assessed in a half-cell configuration with Li metal as a counter electrode. Fig. 4a shows the discharge capacity of identical LFP-based electrodes, fabricated at a substrate temperature of 130 to 180 °C (i.e. a range of morphologies, see Fig. 1), as a function of discharge rate. At a low discharge rate (0.1 C to 2 C), the specific capacities of electrodes sprayed at 160 to 180 °C (well-defined honeycomb pores) were slightly higher than electrodes sprayed at 130 to 150 °C (weak/no honeycomb). When the C rate reached 20 C, the capacities of honeycomb electrodes ($\sim$55 mA h g^{-1}) significantly outperformed non-honeycomb electrodes ($\sim$5 mA h g^{-1}). At 50 C, the 160, 170 and 180 °C substrate honeycomb electrodes had capacities of 33 mA h g^{-1}, 24 mA h g^{-1} and 21 mA h g^{-1}
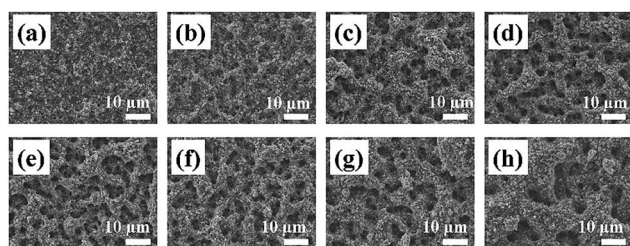

Fig. 3 SEM images of the surface morphology of spray printed LFP-based electrodes as a function of total mass fraction (C) in the suspension of (a) 0.05 g/100 ml, (b) 0.10 g/100 ml, (c) 0.15 g/100 ml, (d) 0.20 g/100 ml, (e) 0.25 g/100 ml, (f) 0.30 g/100 ml, (g) 0.40 g/100 ml and (h) 0.50 g/100 ml.
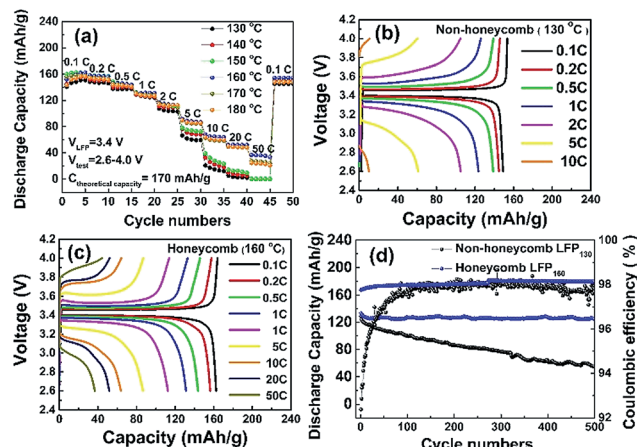

Fig. 4 (a) C-rate capability of non-honeycomb (NH) LFP-based electrodes formed at substrate temperatures of 130 to 150 °C and honeycomb (H) LFP-based electrodes formed at substrate temperatures of 160 to 180 °C; charge and discharge curves for the (b) H electrode and (c) NH electrode, and (d) long-term stability and coulombic efficiency of NH and H electrodes.

respectively while the non-honeycomb electrodes were effectively useless. Given other differences between the electrodes were slight, the improved dynamic response of the honeycomb electrodes was related to the comparative ease of Li ion penetration into the electrode and access to all the active material surface area. In terms of volumetric capacity shown in Fig. S3,† the relative high pore fraction of the honeycomb structure was only beneficial at the highest C rates where the disadvantage of low coating weight (high porosity) was offset by the advantage of delivering Li ions to a greater proportion of the active material.[33] The volumetric capacity for non-honeycomb and honeycomb electrodes was 368 mA h cm^{-3} and 275 mA h cm^{-3} at 0.1 C, reducing to 0 and 62 mA h cm^{-3} at 50 C, as shown in Fig. S3.† In subsequent results, only the 130 °C non-honeycomb (NH) and the 160 °C honeycomb (H) are considered and compared.

Fig. 4b and c show the charge and discharge profiles of the NH and H electrodes at various C rates. At 0.1 C, both electrodes had a flat potential plateau at $\sim$3.4 V corresponding to the redox reaction of the Fe^{3+}/Fe^{2+} couple.[34] The voltage differences between the charge and discharge curves at 0.1 C for NH and H electrodes were 71 mV and 57 mV, respectively. This voltage difference increased to 223 mV and 132 mV at 1 C, and increased further at higher C rates. Overall, for the same charge and discharge rate conditions, the potential plateau of the H electrode was flatter and longer and the polarization smaller when compared with those of the NH electrode, which suggested that the honeycomb structure had a lower charge transfer resistance, which is characterised further later.

The cycling performance of the LFP-based electrodes was investigated up to 500 cycles at 1 C, as shown in Fig. 4d. The H electrode showed greater cycling stability with a 95% capacity retention compared with 55% for the NH electrode. Coulombic efficiencies were $\sim$98% for both electrodes. It was likely that the reduced degradation of the H electrode arose because of the greater fraction of through thickness porosity in this electrode,

19096 | J. Mater. Chem. A, 2019, 7, 19094–19103

This journal is © The Royal Society of Chemistry 2019

which better facilitated the homogenization of the spatial distribution of Li ion concentration. Under these conditions, the accommodation of any volume change and associated strain during the intercalation/deintercalation process is more uniform, and less damaging to the electrode structure.[15,16,18]

Fig. 5a and c show the cyclic voltammograms of NH and H electrodes at scan rates from 0.1 to 1 mV s^{-1}. The peak profiles of H electrodes were more symmetric and peak currents greater than those for NH electrodes, suggesting a reduced charge transfer resistance. Fig. 5b and d show the corresponding plots of the peak anodic current as a function of the square root of the scan rate. In both cases, the variation of peak current density was a good linear fit to the square root of the scan rate, and implied that the overall charge/discharge behaviour for both electrodes was diffusion-controlled.[35] Under these conditions an effective Li-ion diffusion coefficient, which expresses the net effect of the various Li ion transport processes operating in the electrode, can be obtained from the gradient of a best-fit line using the Randles–Sevcik equation:[36,37]

$$I_p = 0.4463n \, FAC_0(nFvD_{Li}/RT)^{1/2} \qquad (1)$$

where I_p is the peak current [A], n is the number of electrons transferred, F is the Faraday constant [C mol^{-1}], A is the electrode area [cm^2], C_0 is the molar concentration of the Li-ions in the electrode [mol cm^{-3}], v is the scan rate [V s^{-1}], D_{Li} is the Li-ion diffusion coefficient [cm^2 s^{-1}], R is the gas constant [J/K mol] and T is the temperature [K].

The Li-ion diffusion coefficients were estimated at 1.5×10^{-11} cm^2 s^{-1} and 3×10^{-11} cm^2 s^{-1} for NH and H electrodes, respectively. Consistent with their higher pore fraction (and low electrode density), the diffusion coefficients were similar or slightly higher than those of similar materials,[38] such as 1.8×10^{-14} cm^2 s^{-1} for a conventional LFP electrode,[39] 2.52×10^{-11} cm^2 s^{-1} for a 3D porous LFP electrode[35] and 6.3×10^{-13} cm^2 s^{-1} for a porous LFP/carbon nanotube composite electrode.[40]

Solid electrolyte-based battery performance. Having established that the baseline performance of both non-honeycomb and honeycomb electrodes in half cells with a conventional electrolyte was sensible and consistent with the literature, in this and subsequent sections the liquid electrolyte was replaced by a spray printed hybrid PEO-LAGP electrolyte. The intention was to assemble various configurations of the electrode and electrolyte materials in a single uninterrupted operation by spray printing, with no need for post fabrication heating or calendaring.

Four different configurations were investigated, which are shown schematically in the Experimental section (Fig. 11):

• NH (non-honeycomb), shown in Fig. 11 (b): five spray printed layers of non-honeycomb LFP (formed at a substrate temperature of 130 °C), immediately followed by ten spray printed layers of PEO-LAGP electrolyte.

• NH-L (non-honeycomb, layered), shown in Fig. 11 (c): one spray printed layer of non-honeycomb LFP, one layer of PEO-LAGP, repeated five times, immediately followed by five layers of PEO-LAGP.

• H (honeycomb), shown in Fig. 11 (d): five layers of honeycomb LFP (formed at a substrate temperature of 160 °C), immediately followed by ten layers of PEO-LAGP.

• H-L (honeycomb, layered), shown in Fig. 11 (e): one spray printed layer of honeycomb LFP, one layer of PEO-LAGP, repeated five times, immediately followed by five layers of PEO-LAGP.

The relatively small diameter of the LAGP particles (~500 nm) and LFP particles (~1 μm) facilitated the deposition of
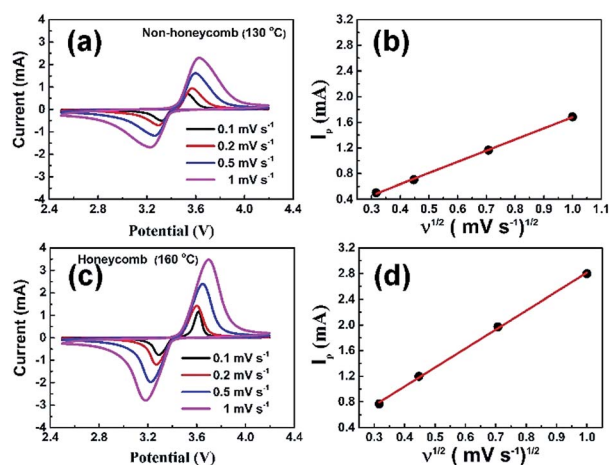

Fig. 5 (a) Cyclic voltammograms for a NH LFP-based electrode and (b) the corresponding best-fit linear relationship between peak current and the square root of the scan rate; (c) and (d) similar plots for a H LFP-based electrode.
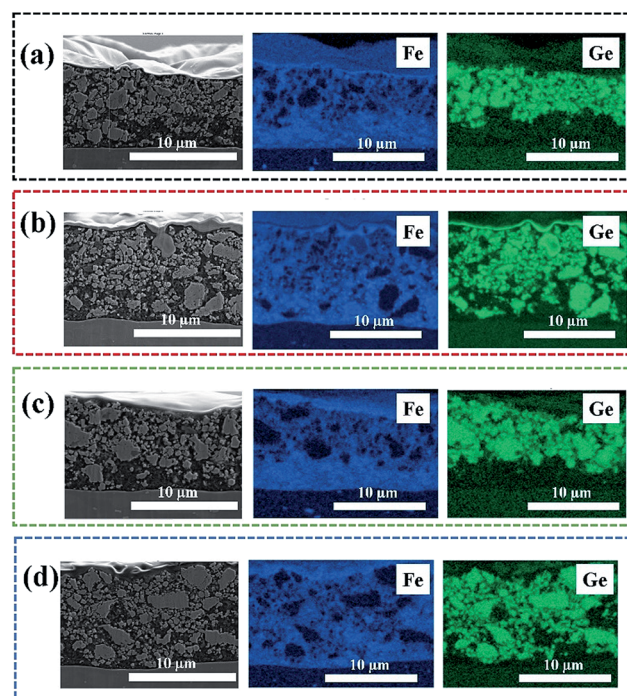

Fig. 6 SEM cross-sectional images of electrodes (a) NH, (b) NH-L, (c) H and (d) H-L, in each case with corresponding EDX maps for elements Fe and Ge that allowed discrimination between LiFePO$_4$ and LAGP particulates, respectively. The current collector is at the bottom.

This journal is © The Royal Society of Chemistry 2019

J. Mater. Chem. A, 2019, 7, 19094–19103 | 19097

relatively thin sub-layers, so that fine-scale inter-leaving of ~5 μm thick layers was possible. The effectiveness of inter-leaving may be reduced when the layer particle diameter increased, which would increase sub-layer thickness. Comparing NH and NH-L electrodes will show the effect of inter-layering the electrolyte when there were a few or no macro-honeycomb pores in the electrode. Comparing H and H-L electrodes will highlight the effect of inter-layering when the electrode has a greater fraction of honeycomb pores to enable through-layer inter-connectivity.

Fig. 6a to d show cross-sectional SEM images of NH, NH-L, H and H-L electrodes with the Al current collector at the bottom of the image and in each case with corresponding EDX maps for elements Fe and Ge that allow discrimination between LiFePO$_4$ and LAGP particulates, respectively. It was not possible to use a similar EDX approach to identify the PEO-based gel electrolyte, but regions that were neither LiFePO$_4$ nor LAGP rich may be assumed to be either the PEO in the hybrid electrolyte or residual pores. Fig. 6a and c show that for both non-inter-layered electrodes there were two distinct layered regions: a ~10 μm LAGP-rich layer on a ~5 μm LiFePO$_4$-rich layer. In all cases there was some limited inter-mixing between layers (or possible smearing during polishing). The presence of honey-comb pores (Fig. 6c) had no marked effect on the extent of inter-mixing. When inter-layering was introduced as shown in Fig. 6b and d, the electrodes were again ~15 μm thick in total, and although there was some evidence for increased LiFePO$_4$-LAGP inter-mixing, again the presence of the honeycomb structure, in Fig. 6d, did not markedly improve inter-layer inter-connectivity from a microstructural perspective.

Fig. 7a to d show the discharge capacity of the four electrodes at C rates of 0.1 to 1 C at temperatures of (a) 30 °C, (b) 40 °C, (c) 50 °C and (d) 60 °C. Regardless of the temperature and structure, the discharge capacity decreased with increasing C rate due to sluggish Li ion diffusion and increasing polarization,[41] recovering capacity when the C rate was reduced back to 0.1 C. As can be expected, discharge capacities increased with increasing temperature due to faster Li ion diffusion and insertion kinetics.[42] The non-layered, non-honeycomb NH electrode had the lowest discharge capacity of ~45 mA h g^{-1} at
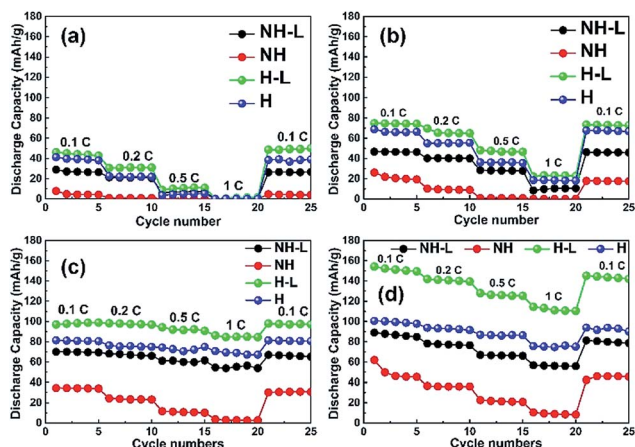

Fig. 7 Discharge capacities of the NH, NH-L, H and H-L electrodes with a hybrid solid-state electrolyte at C rates of 0.1 to 1 C at temperatures of (a) 30 °C, (b) 40 °C, (c) 50 °C and (d) 60 °C.

Fig. 9 Imaginary versus real impedance for the NH, NH-L, H and H-L LFP-based electrodes with a hybrid solid-state electrolyte from Fig. 7 at (a) 30 °C, (b) 40 °C, (c) 50 °C and (d) 60 °C.

Fig. 8 Schematic diagram of the Li-ion mobility within the inter-leaved honeycomb (H-L) electrode.

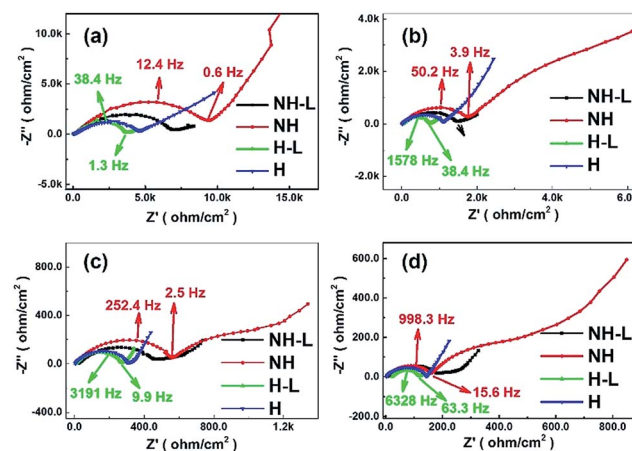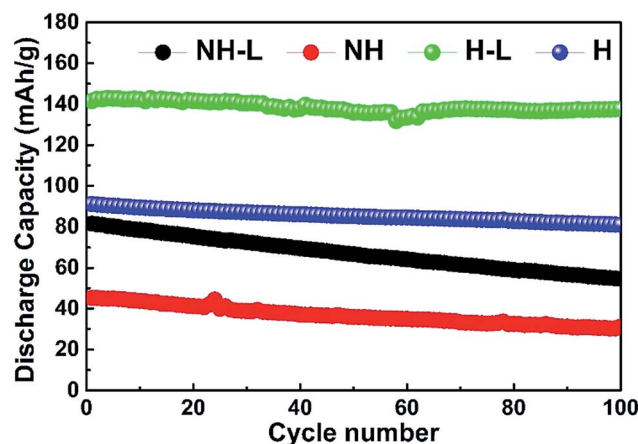Fig. 10 Long-term cycle stability of NH, NH-L, H and H-L LFP-based electrodes with a hybrid PEO-LAGP solid-state electrolyte at 60 °C and 0.1 C.

19098 | J. Mater. Chem. A, 2019, 7, 19094–19103

This journal is © The Royal Society of Chemistry 2019

Table 1 Summary and comparison of solid-state LFP-based electrode performances using an organic–inorganic hybrid electrolyte

Electrode composition (wt%)	Electrolyte composition (wt%)	Discharge capacity (mA h g^{-1})	Long-time discharge capacity retention	Ref.
60LFP + 12SP + 20CPMEA^a + 8LiTFSI^b	CPMEA/LATP^c/CPMEA	130 (65 °C and 0.2 C)	~58% (325 cycles)	28
70LFP + 10SP + 20(PEO-LAGP)	80PEO + 20LAGP-LITFSI	166 (60 °C and 0.1 C)	~90% (50 cycles)	42
55LFP + 30.86PEO + 4.14 LiClO$_4$ + 10SP	30PEO + 70LAGP-LITFSI	137.6 (55 °C and 0.2 C)	88% (100 cycles)	44
50LFP + 30.86PEO + 4.14 LiClO$_4$ + 5SN + 10SP	70LAGP + 21PEO-LiClO$_4$ + 9SN	127.8–136.8 (25 °C and 0.2 C)	98% (100 cycles)	47
85LiNi$_{0.5}$Co$_{0.2}$Mn$_{0.3}$O$_2$ + 7.5PVDF + 7.5SP	90 LAGP + 10(P(VdF-co-HFP)^d) + LiPF$_6$-based liquid electrolyte	157.6 (25 °C and 0.5 C)	86.9% (200 cycles)	48
80LFP + 10SP + 10PVDF + 30PEO-LITFSI-70LAGP (H-L electrode)	30PEO-LITFSI-70LAGP	150 (60 °C and 0.1 C)	97.2% (100 cycles)	This work
80LFP + 10SP + 10PVDF (H electrode)	30PEO-LITFSI-70LAGP	99 (60 °C and 0.1 C)	88.9% (100 cycles)	This work
80LFP + 10SP + 10PVDF + 30PEO-LITFSI-70LAGP (NH-L electrode)	30PEO-LITFSI-70LAGP	85 (60 °C and 0.1 C)	66.9% (100 cycles)	This work
80LFP + 10SP + 10PVDF (NH electrode)	30PEO-LITFSI-70LAGP	45 (60 °C and 0.1 C)	67.3% (100 cycles)	This work

^{a} CPMEA = cross-linked poly(ethylene glycol) methyl ether acrylate. ^{b} LIFTSI = lithium bis(trifluoromethanesulfonyl)imide. ^{c} LATP = Li$_{1.3}$Al$_{0.3}$Ti$_{1.7}$(PO$_4$)$_3$. ^{d} P(VdF-co-HFP) = poly(vinylidene fluoride-co-hexafluoropropylene).

0.1 C that reduced to ∼7 mA h g^{-1} at 1 C; in contrast, the inter-layered, honeycomb H-L electrode comprising exactly the same materials but in a different geometrical arrangement delivered ∼150 mA h g^{-1} at 0.1 C and ∼110 mA h g^{-1} at 1 C, which was almost the same as the closely similar honeycomb electrode in the conventional liquid electrolyte previously shown in Fig. 4. This shows the limitations to inferring likely electrochemical performance from 2D microstructural sections, and implies the actual electrolyte connectivity in 3D was more extensive in the honeycomb electrodes than suggested by the 2D sections. Fig. 8 shows a schematic of the inter-leaved honeycomb (H-L) electrode in which the hybrid solid-state electrolyte has filled the honeycomb pores that penetrate between the LFP-rich layers. The Li ions can thus move relatively easily both within the plane of the electrode, and through the electrode, between layers. It was this enabling of Li mobility to all parts of the electrode that provided its higher capacity. At 30 °C, the capacity of all electrodes was reduced but the trends in relative performance between the different electrodes were the same, with the best-performing H-L electrode delivering a discharge capacity of ∼45 mA h g^{-1} at 0.1 C.

To investigate further the effect of microstructural arrangement on electrode dynamics, Fig. 9 shows Nyquist plots for the four electrode types corresponding to each of the temperatures in the plots in Fig. 7. Each Nyquist plot contained one or two overlapping semi-circles in the high/medium frequency region and inclined lines in the low frequency region. The diameter of a best-fit semi-circle to the data indicates the resistance of the electrode to Li$^+$ ion movement through the solid electrolyte and the charge transfer resistance at the electrode–electrolyte interface, which is the main resistance of all-solid-state batteries. The inclined lines in the low frequency domain represent the Warburg impedance corresponding to Li-ion diffusion behaviour within the electrodes.[42] Approximately, the smaller the semi-circle the lower the transport resistance. Taking the non-honeycomb NH electrode at 60 °C for example, the relatively large diameter semi-circle was likely due to the electrode/electrolyte interface resistance (∼600 Ω) and the smaller semi-circle related to Li-ion diffusion resistance within the electrolyte (∼160 Ω). The total resistance of the NH electrode was much larger than that of the NH-L electrode (∼250 Ω). For the honeycomb-based electrodes H and H-L, there was only one semi-circle in the high/medium frequency range, which suggested that interfacial resistance between the electrode and electrolyte dominated, and the total resistances of the H (∼150 Ω) electrode and the H-L (∼110 Ω) electrode were lower than those of the corresponding NH and NH-L electrodes. Thus, the combination of honeycomb morphology and inter-layering improved interfacial contact between the LFP and PEO-LAGP electrolyte. When tested at lower temperature, the phenomenon of two semi-circles in the high frequency reducing to one became more pronounced.

The cycle stability of the NH, NH-L, H and H-L LFP-base electrodes at 60 °C and 0.1 C is shown in Fig. 10, indicating that both the honeycomb electrodes, whether layered or not, had a lower rate of discharge capacity degradation than their non-honeycomb equivalents. For example, the H-L and H

This journal is © The Royal Society of Chemistry 2019

J. Mater. Chem. A, 2019, 7, 19094–19103 | 19099

electrodes had a capacity of 138 mA h g^{-1} (97.2% retention) and 81 mA h g^{-1} (88.9% retention), respectively, after 100 continuous cycles whereas the NH-L and NH equivalents had a capacity of 55 mA h g^{-1} (66.9% retention) and 31 mA h g^{-1} (67.3% retention), respectively. Considering the behaviour shown in Fig. 7 and 8, the relatively high capacity retention of the honeycomb electrode, especially the H-L electrode, is most likely related to the compliance provided throughout the electrode by the inter-layered hybrid PEO-LAGP electrolyte, which helped to ensure that electrode/electrolyte contact was maintained during the volume change of the LFP during intercalation/deintercalation cycles.[15,18]
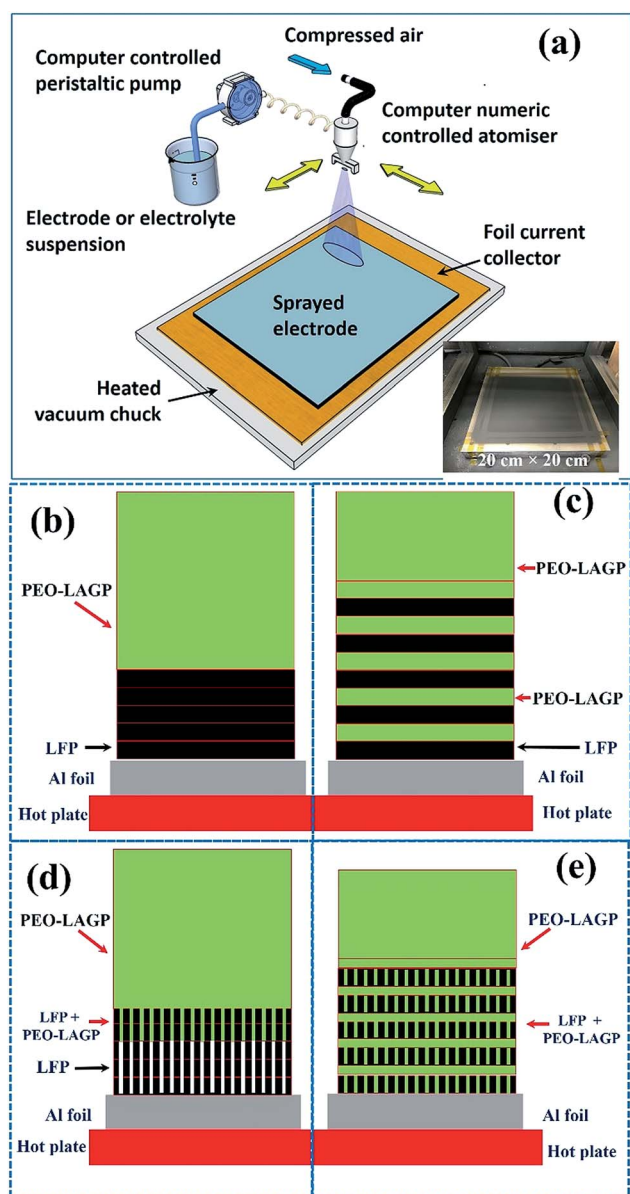

Fig. 11 Schematic diagrams of (a) spray printing, and spray printing four different electrodes of (b) NH (non-honeycomb), (c) NH-L (non-honeycomb, layered), (d) H (honeycomb) and (e) H-L (honeycomb, layered). LFP = LiFePO$_4$, SP = super P carbon, PVDF = polyvinylidene fluoride, PEO-LAGP = hybrid electrolyte, PEO = polyethylene oxide and LAGP = Li$_{1.5}$Al$_{0.5}$Ge$_{1.5}$(PO$_4$)$_3$.

Overall, the solid-state LFP-based H-L electrode half cell performance was similar or better than previous reports,[29,42–56] as summarized in Table 1. In these prior studies, the fabrication of the electrode and fabrication of the electrolyte were separate, and were usually combined with post fabrication heating and drying as well as post-assembly processes to prepare cells. Here, co-spray printing prepared the electrode and electrolyte structures directly with minimized post processing, and allowed both inter-layering and honeycomb pores, both of which promoted improved performance. Spray printing is a general propose approach suitable for many other cathode, anode and electrolyte materials, and for electrode thicknesses up to 100s of μm. Thus, the direct production of full solid-state inter-layered cathode–electrolyte–anode cells can be easily envisaged.[32]

Conclusions

Honeycomb LFP electrodes (H) were successfully prepared by spray printing at a substrate temperature ≥160 °C using a 10 vol% NMP/IPA solvent ratio and a 0.25 g/100 ml suspension concentration. For liquid electrolyte batteries, the honeycomb electrodes improved rate cycling performance at 5 C or higher. At 50 C, a honeycomb electrode delivered a capacity of 33 mA h g^{-1} while non-honeycomb electrodes were effectively useless. After 500 cycles at 1 C, the honeycomb electrode had 95% capacity retention. The lithium-ion mobility in the honeycomb electrode was approximately twice that of the non-honeycomb electrode. For a solid-state half cell using a spray printed PEO-LAGP hybrid electrolyte, inter-leaving the electrolyte inside a honeycomb electrode produced the best rate performance and long-term cycle stability, e.g. 150 mA h g^{-1} at 0.1 C and 97.2% retention after 100 continuous cycles at 60 °C. Cross-sectional SEM and EDS mapping combined with EIS testing suggested that the honeycomb morphology and inter-leaving improved interfacial contact between the electrode and solid-state electrolyte. The spray printing process is relatively straightforward to scale up and could provide a direct route for the fabrication of practical solid-state batteries.

Experimental

Preparation of cathode and electrolyte suspension

Particulate LFP and Super P (SP) carbon black to promote electrical conductivity were obtained from MTI Corporation, USA and polyvinylidene fluoride (PVDF) binder, N-methyl-2-pyrrolidone (NMP) and isopropyl alcohol (IPA) were obtained from Sigma-Aldrich, UK. All powders were dried in an oven for > 24 hours at 60 °C before electrode suspension preparation and used directly without any further treatment. For a typical LFP cathode suspension for spray printing, 0.2 g LFP, 0.025 g SP and 0.025 g PVDF were mixed with 10 ml NMP and the resulting suspension stirred magnetically for 30 min. Then, 90 ml IPA was added and stirred for a further 30 min. The suspension was then ultrasonicated for 30 min after which a dilute stable suspension with no settling of solids over several hours was obtained, suitable for pumping and atomisation during spray printing.

19100 | J. Mater. Chem. A, 2019, 7, 19094–19103

This journal is © The Royal Society of Chemistry 2019

For the hybrid electrolyte suspension suitable for spray printing, a 30 wt% PEO-70 wt% LAGP mixture was chosen based on prior work.[44] Dried LITFSI (100 °C for 24 h, Sigma-Aldrich) as the Li salt was combined with PEO (M_n = 4 000 000 and melting point ~65 °C, Sigma-Aldrich) at a PEO : Li^+ ratio of 18 : 1. LAGP powder with a number mean particle diameter of approximately 500 nm (MTI Corporation, USA) was incorporated into the hybrid electrolyte as follows: 0.3 g PEO, 0.236 g LITFSI and 0.7 g LAGP were placed in a dry beaker, 10 ml anhydrous acetonitrile and 90 ml IPA were added, followed by stirring and ultra-sonication as described for the LFP suspension above.

Spray printing

The LFP-based electrode was fabricated using a spray printing technique developed in our group for various electrochemical energy storage applications, described in detail elsewhere[31,32,57–64] and shown schematically in Fig. 11a. 80 mm × 80 mm Al current collector foil was attached to a vacuum chuck substrate and secured with polyimide tape. The various suspensions were peristaltically pumped at typically 5 ml min^{-1} and atomised in an industrial spray nozzle using compressed air at 0.2 bar while simultaneously reciprocating in a pre-programmed pattern over the current collector in the x–y plane at a constant distance of 15 cm. The printed area was 100 mm × 100 mm to ensure that all the foil was coated evenly. As the sprayed suspension droplets deposited on the hot current collector, the NMP and IPA fugitive carriers evaporated almost immediately so that there was no build-up of liquid in the forming electrode and no substantive re-suspension of previously deposited layers. After printing, the coated foils were dried in a vacuum oven at 120 °C overnight for subsequent characterization or coin cell assembly.

Two different spray printing strategies shown schematically in Fig. 11 (b) and (c) were investigated. First, the LFP electrode (thickness ~5 μm) was formed from the LFP-based suspension only, and then a hybrid PEO-LAGP layer (thickness ~10 μm) was printed on top, as shown in Fig. 11b. Second, much thinner layers (~1 μm) of LFP and PEO-LAGP were repeatedly interleaved to form the multi-layer electrode arrangement shown schematically in Fig. 11c. For a fair comparison between the two arrangements, the total number of sprayed layers of the LFP suspension was fixed at 5 and the PEO-LAGP suspension fixed at 10, regardless of the order in which the layers were deposited. Fig. 11d and e show similar electrode cross-sections but in the case of honeycomb layers. In Fig. 11d, it is anticipated that at least partial infiltration of honeycomb pores by the hybrid electrolyte will occur; in Fig. 11e, the use of inter-layering may allow the filled pores to bridge between the inter-layers of the hybrid electrolyte. Further, the filling of the pores in the thin LFP layers with the PEO-LAGP electrolyte will also likely provide an increase in the overall active material surface area that is relatively easy for the charge carrying ions in the electrolyte to access. Overall, the arrangement in Fig. 11e aims to boost the electrode capacity and dynamic response by a combination of greater continuity and inter-penetration of the electrolyte together with an increase in active/electrolyte area. The total

coating weights of the LFP and LFP–PEO–LAGP electrodes were 3.6 mg cm^{-2} and 6 mg cm^{-2}, respectively.

Electrode characterization

A microbalance (Sartorius, Germany) with 0.1 mg accuracy was used for weighing electrode materials and a screw micrometer (IP65 Coolant Proof, Mitutoyo, Japan) was used to measure the electrode thickness. The electrode surface morphology and cross-sectional microstructure were characterized by scanning electron microscopy (SEM, JEOL 6500F, Japan). For cross-sectional images, a Gatan Precision Etching Coating System (PECS 685) was used for polishing with a 6 keV beam and 2 h milling. Energy-dispersive X-ray spectroscopy (EDS) mapping using a field emission gun SEM (Carl Zeiss Merlin, Germany) was used to distinguish between LFP regions (Fe signal) and PEO-LAGP regions (Ge signal).

Battery assembly and electrochemical characterization

2032 coin-type half-cells were assembled in an Ar-filled glove box with water and oxygen levels lower than 1 ppm using 16 mm discs punched from LFP or LFP–PEO(LITFSI)-LAGP coated foils. Lithium chips of 15.5 mm diameter and 0.5 mm thickness were used at the counter/reference electrode. A Li chip was directly placed on the top of the two layers of the LFP-based cathode plus the PEO(LITFSI)-LAGP hybrid electrolyte. For electrodes investigated in a liquid electrolyte, a 25 μm thick trilayer polypropylene–polyethylene–polypropylene membrane separator (Celgard, USA) and a 1 M $LiPF_6$ solution in a mixture of ethylene carbonate (EC) and dimethyl carbonate (DMC) at a volume ratio of 1 : 1 electrolyte was used. All half-cells were investigated during galvanostatic charge/discharge between 4.2 and 2.6 V (*versus* Li/Li$^+$) at various C rates from 0.1 to 1 C (solid electrolyte) or 50 C (liquid electrolyte) using a battery cycler (Arbin BT-G-25, USA) as a function of temperature, including long-term cycling behaviour. Cyclic voltammetry was performed between 2.5 and 4.2 V at scan rates from 0.1 to 1 mV s^{-1} using a potentiostat/galvanostat (Gamry Reference 600/EIS300). Electrochemical impedance spectroscopy (EIS) was also conducted in the range 10^5 to 0.01 Hz with an applied oscillating voltage of 10 mV at open circuit potential.

Conflicts of interest

There are no conflicts to declare.

Acknowledgements

References

1 A. F. Burke, *Proc. IEEE*, 2007, **95**, 806–820.

2 A. Khaligh and Z. H. Li, *IEEE Trans. Veh. Technol.*, 2010, **59**, 2806–2814.

3 J. Janek and W. G. Zeier, *Nat. Energy*, 2016, **1**, 16141.

4 B. Kang and G. Ceder, *Nature*, 2009, **458**, 190–193.

5 S. Choi, T. H. Kim, J. I. Lee, J. Kim, H. K. Song and S. Park, *ChemSusChem*, 2014, **7**, 3483–3490.

6 Y. Hirotoshi, *J. Indian Inst. Sci.*, 2016, **96**, 315–324.

7 C. H. Jiang, E. Hosono and H. S. Zhou, *Nano Today*, 2006, **1**, 28–33.

8 Y.-G. Guo, J.-S. Hu and L.-J. Wan, *Adv. Mater.*, 2008, **20**, 2878–2887.

9 H. Li, Z. X. Wang, L. Q. Chen and X. J. Huang, *Adv. Mater.*, 2009, **21**, 4593–4607.

10 S. Goriparti, E. Miele, F. De Angelis, E. Di Fabrizio, R. P. Zaccaria and C. Capiglia, *J. Power Sources*, 2014, **257**, 421–443.

11 Y. Yu, C. H. Chen, J. L. Shui and S. Xie, *Angew. Chem., Int. Ed.*, 2005, **44**, 7085–7089.

12 M. Yao, K. Okuno, T. Iwaki, M. Kato, S. Tanase, K. Emura and T. Sakai, *J. Power Sources*, 2007, **173**, 545–549.

13 H. Zhang, X. Yu and P. V. Braun, *Nat. Nanotechnol.*, 2011, **6**, 277–281.

14 L. Hu, H. Wu, Y. Gao, A. Cao, H. Li, J. McDough, X. Xie, M. Zhou and Y. Cui, *Adv. Energy Mater.*, 2011, **1**, 523–527.

15 H. Ji, L. Zhang, M. T. Pettes, H. Li, S. Chen, L. Shi, R. Piner and R. S. Ruoff, *Nano Lett.*, 2012, **12**, 2446–2451.

16 B. Wang, W. Al Abdulla, D. L. Wang and X. S. Zhao, *Energy Environ. Sci.*, 2015, **8**, 869–875.

17 S. Wi, J. Kim, K. Park, S. Lee, J. Kang, K. H. Kim, S. Nam, C. Kim and B. Park, *RSC Adv.*, 2016, **6**, 105081–105086.

18 Y. K. Zhou, J. M. Lu, C. J. Deng, H. X. Zhu, G. Z. Chen, S. W. Zhang and X. H. Tian, *J. Mater. Chem. A*, 2016, **4**, 12065–12072.

19 J. G. Kim, B. Son, S. Mukherjee, N. Schuppert, A. Bates, O. Kwon, M. J. Choi, H. Y. Chung and S. Park, *J. Power Sources*, 2015, **282**, 299–322.

20 J. W. Fergus, *J. Power Sources*, 2010, **195**, 4554–4569.

21 E. Quartarone and P. Mustarelli, *Chem. Soc. Rev.*, 2011, **40**, 2525–2540.

22 S. Teng, J. J. Tan and A. Tiwari, *Curr. Opin. Solid State Mater. Sci.*, 2014, **18**, 29–38.

23 Y. Xiayin, H. Bingxin, Y. Jingyun, P. Gang, H. Zhen, G. Chao, L. Deng and X. Xiaoxiong, *Chin. Phys. B*, 2016, **25**, 018802.

24 J. C. Bachman, S. Muy, A. Grimaud, H. H. Chang, N. Pour, S. F. Lux, O. Paschos, F. Maglia, S. Lupart, P. Lamp, L. Giordano and Y. Shao-Horn, *Chem. Rev.*, 2016, **116**, 140–162.

25 L. Fan, S. Wei, S. Li, Q. Li and Y. Lu, *Adv. Energy Mater.*, 2018, **8**, 1702657.

26 S. Ramakumar, C. Deviannapoorani, L. Dhivya, L. S. Shankar and R. Murugan, *Prog. Mater. Sci.*, 2017, **88**, 325–411.

27 Z. G. Xue, D. He and X. L. Xie, *J. Mater. Chem. A*, 2015, **3**, 19218–19253.

28 W. Zhou, S. Wang, Y. Li, S. Xin, A. Manthiram and J. B. Goodenough, *J. Am. Chem. Soc.*, 2016, **138**, 9385–9388.

29 Y. Li, B. Xu, H. Xu, H. Duan, X. Lu, S. Xin, W. Zhou, L. Xue, G. Fu, A. Manthiram and J. B. Goodenough, *Angew. Chem., Int. Ed.*, 2017, **56**, 753–756.

30 L. Chen, Y. Li, S.-P. Li, L.-Z. Fan, C.-W. Nan and J. B. Goodenough, *Nano Energy*, 2018, **46**, 176–184.

31 S. H. Lee, A. Mahadevegowda, C. Huang, J. D. Evans and P. S. Grant, *J. Mater. Chem. A*, 2018, **6**, 13133–13141.

32 S. H. Lee, C. Huang, C. Johnston and P. S. Grant, *Electrochim. Acta*, 2018, **292**, 546–557.

33 N. Nitta, F. X. Wu, J. T. Lee and G. Yushin, *Mater. Today*, 2015, **18**, 252–264.

34 L. X. Yuan, Z. H. Wang, W. X. Zhang, X. L. Hu, J. T. Chen, Y. H. Huang and J. B. Goodenough, *Energy Environ. Sci.*, 2011, **4**, 269–284.

35 X. F. Tu, Y. K. Zhou and Y. J. Song, *Appl. Surf. Sci.*, 2017, **400**, 329–338.

36 D. Di Lecce and J. Hassoun, *J. Phys. Chem. C*, 2015, **119**, 20855–20863.

37 H. Guo, X. D. Zhang, W. He, X. N. Yang, Q. Z. Liu, M. Li and J. C. Wang, *RSC Adv.*, 2016, **6**, 16933–16940.

38 M. Park, X. C. Zhang, M. D. Chung, G. B. Less and A. M. Sastry, *J. Power Sources*, 2010, **195**, 7904–7929.

39 P. P. Prosini, M. Lisi, D. Zane and M. Pasquali, *Solid State Ionics*, 2002, **148**, 45–51.

40 Y. Zhou, J. Wang, Y. Hu, R. O'Hayre and Z. Shao, *Chem. Commun.*, 2010, **46**, 7151–7153.

41 M. Broussely, P. Biensan, F. Bonhomme, P. Blanchard, S. Herreyre, K. Nechev and R. J. Staniewicz, *J. Power Sources*, 2005, **146**, 90–96.

42 Y. R. Zhao, Z. Huang, S. J. Chen, B. Chen, J. Yang, Q. Zhang, F. Ding, Y. H. Chen and X. X. Xu, *Solid State Ionics*, 2016, **295**, 65–71.

43 H. Zhou, Y. Wang, H. Li and P. He, *ChemSusChem*, 2010, **3**, 1009–1019.

44 Y. C. Jung, S. M. Lee, J. H. Choi, S. S. Jang and D. W. Kim, *J. Electrochem. Soc.*, 2015, **162**, A704–A710.

45 M. R. Busche, T. Drossel, T. Leichtweiss, D. A. Weber, M. Falk, M. Schneider, M. L. Reich, H. Sommer, P. Adelhelm and J. Janek, *Nat. Chem.*, 2016, **8**, 426–434.

46 P. He, T. Zhang, J. Jiang and H. Zhou, *J. Phys. Chem. Lett.*, 2016, **7**, 1267–1280.

47 Y. C. Jung, M. S. Park, C. H. Doh and D. W. Kim, *Electrochim. Acta*, 2016, **218**, 271–277.

48 S. K. Kim, Y. C. Jung, D. H. Kim, W. C. Shin, M. Ue and D. W. Kim, *J. Electrochem. Soc.*, 2016, **163**, A974–A980.

49 S. Gu, X. Huang, Q. Wang, J. Jin, Q. S. Wang, Z. Y. Wen and R. Qian, *J. Mater. Chem. A*, 2017, **5**, 13971–13975.

50 M. Keller, G. B. Appetecchi, G.-T. Kim, V. Sharova, M. Schneider, J. Schuhmacher, A. Roters and S. Passerini, *J. Power Sources*, 2017, **353**, 287–297.

51 Q. Pan, D. Barbash, D. M. Smith, H. Qi, S. E. Gleeson and C. Y. Li, *Adv. Energy Mater.*, 2017, **7**, 1701231.

52 M. Cheng, Y. Jiang, W. Yao, Y. Yuan, R. Deivanayagam, T. Foroozan, Z. Huang, B. Song, R. Rojaee, T. Shokuhfar,

Y. Pan, J. Lu and R. Shahbazian-Yassar, *Adv. Mater.*, 2018, **30**, e1800615.

53 M. Keller, A. Varzi and S. Passerini, *J. Power Sources*, 2018, **392**, 206–225.

54 M. S. Park, Y. C. Jung and D. W. Kim, *Solid State Ionics*, 2018, **315**, 65–70.

55 W. Q. Zhang, J. H. Nie, F. Li, Z. L. Wang and C. Q. Sun, *Nano Energy*, 2018, **45**, 413–419.

56 Y. W. Zheng, Q. W. Pan, M. Clites, B. W. Byles, E. Pomerantseva and C. Y. Li, *Adv. Energy Mater.*, 2018, **8**, 1801885.

57 X. Zhao, B. T. Chu, B. Ballesteros, W. Wang, C. Johnston, J. M. Sykes and P. S. Grant, *Nanotechnology*, 2009, **20**, 065605.

58 C. Huang, N. Grobert, A. A. R. Watt, C. Johnston, A. A. R. Watt, C. Johnston, A. Crossley, N. P. Young and P. S. Grant, *Carbon*, 2013, **61**, 525–536.

59 C. Huang and P. S. Grant, *Sci. Rep.*, 2013, **3**, 2393.

60 C. Huang, N. P. Young and P. S. Grant, *J. Mater. Chem. A*, 2014, **2**, 11022–11028.

61 C. Huang, J. Zhang, H. J. Snaith and P. S. Grant, *ACS Appl. Mater. Interfaces*, 2016, **8**, 20756–20765.

62 C. Huang, J. Zhang, N. P. Young, H. J. Snaith and P. S. Grant, *Sci. Rep.*, 2016, **6**, 25684.

63 C. Huang, N. P. Young, J. Zhang, H. J. Snaith and P. S. Grant, *Nano Energy*, 2017, **31**, 377–385.

64 C. Huang and P. S. Grant, *J. Mater. Chem. A*, 2018, **6**, 14689–14699.

This journal is © The Royal Society of Chemistry 2019

J. Mater. Chem. A, 2019, **7**, 19094–19103 | **19103**